

# A Family of IPT Battery Chargers With Small Clamp Coil for Configurable and Self-Sustained Battery Charging Profile

Chunwei Ma<sup>1</sup>, Student Member, IEEE, Ruoyu Yao, Cheng Li, and Xiaohui Qu<sup>2</sup>, Senior Member, IEEE

**Abstract**—To self-sustain the constant current (CC) output to constant voltage (CV) output transition for inductive power transfer (IPT) chargers, the clamp coil-assisted IPT battery chargers are better than the existing solutions due to the merits of no additional switching components, sensors, and control circuits. However, the clamp coil of these IPT chargers is bulky and hard to design, as the mutual inductances between the clamp coil and the main coupler coils are significant to the output performances. To facilitate the small clamp coil in the transmitter, this article proposes a family of IPT battery chargers with a proper second-order compensation network on the secondary side. The output thresholds of the IPT charger with the proper compensation can be readily configured to cope with the desired charging profile, and the clamp coil can be designed very small to decrease the corresponding cost and size. In addition, the proposed three-coil IPT charger still features automatic and smooth CC-to-CV transition to eliminate wireless communication, near unity power factor to minimize voltage-ampere ratings, soft switching to improve transfer efficiency, and open-circuit protection during CC charging. An experimental prototype of a 48 V/2.5 A battery charger is built to verify the analysis.

**Index Terms**—Battery charger, clamp coil, configurable output, inductive power transfer (IPT), self-sustained constant current (CC) to constant voltage (CV) transition.

## I. INTRODUCTION

AS AN alternative to the traditional plug-and-play method of power supply, inductive power transfer (IPT) technology has evolved significantly in the past decades. Through weak magnetic coupling, the IPT system can transfer power over a short distance. Owing to this advantage, the IPT battery charging technology has been widely applied in applications, such as consumer electronics [1], [2], bioimplants [3], [4], electric vehicles (EVs) [5], [6], and industrial equipment [7], [8], [9].

Manuscript received 7 December 2022; revised 14 February 2023; accepted 9 March 2023. Date of publication 15 March 2023; date of current version 20 April 2023. This work was supported by the National Natural Science Foundation of China under Grant 52077038. Recommended for publication by Associate Editor D. Dujic. (Corresponding author: Xiaohui Qu.)

Chunwei Ma, Cheng Li, and Xiaohui Qu are with the School of Electrical Engineering, Southeast University, Nanjing 210096, China, and also with the Jiangsu Key Laboratory of Smart Grid Technology and Equipment, Southeast University, Nanjing 210096, China (e-mail: machunwei@seu.edu.cn; 374743256@qq.com; xhqu@seu.edu.cn).

Ruoyu Yao is with the State Grid Shanghai Pudong Electric Power Supply Company, Shanghai 200120, China (e-mail: yaory2018@outlook.com).

Color versions of one or more figures in this article are available at <https://doi.org/10.1109/TPEL.2023.3257372>.

Digital Object Identifier 10.1109/TPEL.2023.3257372

To effectively charge lithium-ion batteries, the IPT battery charger should provide an initial constant current (CC) and a subsequent constant voltage (CV) output. However, a single-stage IPT converter with a single topology and simple control scheme is only capable of providing either CC or CV output [10]. To implement the CC-to-CV transition for the battery chargers, it is an intuitive idea to form a multistage system by cascading dc/dc converters. In [11] and [12], a dc/dc converter is cascaded at the front or back end of the IPT converter, where the CC-to-CV transition of chargers is achieved by switching the current control loop to the voltage control loop. Another solution to achieve the CC-to-CV transition is by changing the conduction modes of two compensation tanks that have the inherent load-independent CC and CV outputs at the same operating frequency, respectively [13], [14]. But several bidirectional ac switches are needed in this hybrid IPT system. The research in [15] and [16] reveals that if the compensation circuit is high order enough, such as double-sided LCC topology, there are two or more resonant frequencies for load-independent CC and CV outputs. Thus, the CC-to-CV transition can be readily implemented by the frequency hopping control. Besides, variable compensation inductors and capacitors can also be used to adjust the output transconductance or voltage gain of the IPT system to match the required battery charge profile [17], [18]. However, the aforementioned methods usually require additional components, necessary sensors, and complex controls for precise CC-to-CV transition. Therefore, the extra cost, volume, and low reliability are inevitable.

It is better to realize the CC-to-CV transition automatically, such that additional sensors and complex controls can be saved. By introducing an assistive clamp coil and a passive diode rectifier bridge in the transmitter or receiver, the three-coil-based IPT converters were proposed [19], [20]. Obviously, the assistive coil and rectifier located on the receiver will increase the volume and weight of charging devices, for example, EVs. Therefore, it is simpler and more convenient to use a primary clamp coil, such as the S(series)-S-S-based IPT charger proposed in [20]. This charger can provide the input near zero-phase angle (ZPA) and soft switching for all switches in both CC and CV charging modes. Moreover, open-circuit protection is featured during CC charging. However, the output voltage in the simple S-S-S compensation network relies greatly on the parameters of the three-coil magnetic coupler, making the clamp coil bulky and hard to design.

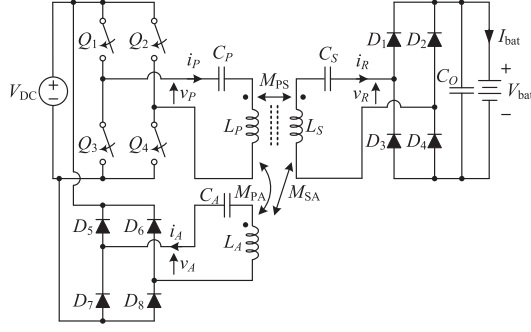


Fig. 1. Clamp coil-assisted S-S-S IPT battery charger in [20].

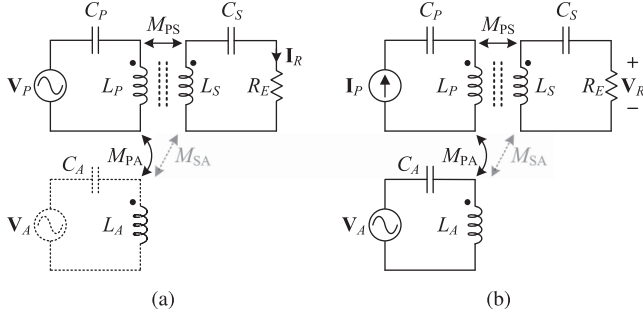


Fig. 2. Equivalent circuits for two different modes. (a) CC mode. (b) CV mode.

To combat the constraints of coupler parameters, a family of IPT battery chargers with a small clamp coil is proposed to realize the automatic CC-to-CV charging transition. By analyzing the features of the primary side's drive source in different modes, the compensation networks' matrix characteristics combating coupler parameter constraints of these chargers are presented. Based on these characteristics, the clamp coil of the proposed charger can be designed very small and placed inside the primary coil that almost does not increase the size of the magnetic coupler. Besides, the unexpected coupling between the clamp coil and secondary coil is corresponding small to decrease the practical effect of the output voltage. Especially, these chargers still feature automatic and smooth CC-to-CV transition to eliminate wireless communication, near unity power factor to minimize voltage-ampere (VA) ratings, soft switching to improve transfer efficiency, and open-circuit protection during CC charging. An experimental prototype with 48 V/2.5 A output is built to validate the performances of the proposed IPT charger.

## II. DERIVATION OF COMPENSATION NETWORKS COMBATING TRANSFORMER PARAMETER CONSTRAINTS

### A. Limitation of the S-S-S-Based IPT Charger

To point out the limitation of clamp coil-assisted S(primary)-S(secondary)-S(auxiliary) IPT charger in [20], Fig. 1 and its equivalent circuit Fig. 2 are given here, where  $L_P$ ,  $L_S$ , and  $L_A$  are the self-inductances of primary, secondary, and clamp coils,  $M_{PS}$ ,  $M_{PA}$ , and  $M_{SA}$  are the mutual inductances between the three coils, and  $C_P$ ,  $C_S$ , and  $C_A$  are series compensation

capacitors.  $R_L = \frac{V_{bat}}{I_{bat}}$  is the equivalent resistance of the battery, which gradually increases with state-of-charge (SOC) during the charging process. The resonant frequencies of the primary, secondary, and auxiliary sides are all set to the same value as the switching frequency  $\omega = 2\pi f = \frac{1}{\sqrt{L_P C_P}} = \frac{1}{\sqrt{L_S C_S}} = \frac{1}{\sqrt{L_A C_A}}$ . The voltage  $v_P$  is chopped from the dc voltage  $V_{dc}$  with the inverter of phase shift angle  $\alpha$ , i.e.,

$$|V_P| = \frac{4}{\pi} V_{dc} \sin \frac{\alpha}{2}. \quad (1)$$

With the assumption that  $M_{SA}$  is small enough to be negligible, the relationship of the resonant network voltage vectors in Fig. 2 can be obtained as

$$\begin{cases} V_P = -j\omega M_{PS} I_R - j\omega M_{PA} I_A & (2a) \\ V_R = j\omega M_{PS} I_P = I_R R_E & (2b) \\ V_A = j\omega M_{PA} I_P & (2c) \end{cases}$$

where  $|V_R| = \frac{4V_{BAT}}{\pi}$  and  $R_E = \frac{8R_L}{\pi^2}$ .

Based on (2b) and (2c), as the voltage of battery  $V_{BAT}$  is not large enough to make the induced voltage  $v_A$  by  $I_P$  exceed  $V_{dc}$  at the beginning of charging, the auxiliary circuit is not activated, i.e.,  $i_A = 0$ . Thus, the CC charging starts with the S(primary)-S(secondary) compensated IPT converter, as shown in Fig. 2(a), and the CC output is generated as

$$I_R = \frac{V_P}{j\omega M_{PS}}. \quad (3)$$

As the charging persists,  $v_A$  reaches  $V_{dc}$  with the increase of  $R_E$ , and the auxiliary circuit is activated. Thus, the amplitude of  $v_A$  is clamped by the diodes  $D_{5-8}$  at  $|V_A| = \frac{4V_{dc}}{\pi}$ . Based on (2c), an equivalent current source  $I_P = \frac{V_A}{j\omega M_{PA}}$  drives the main circuit, as shown in Fig. 2(b). Then, a CV output is given as

$$V_R = j\omega M_{PS} I_P = \frac{M_{PS}}{M_{PA}} V_A. \quad (4)$$

By (3) and (4), the CC and CV outputs in two modes are restricted by the mutual inductances  $M_{PS}$  and  $M_{PA}$ . Therefore, the three-coil S-S-S-based IPT charger has no freedom to design the configurable charging profile. In other words, if the main coupling is fixed, the clamp coil should be designed according to the battery charging profile, which makes it hard to design, especially in some space-constrained applications.

### B. Derivation of High-Order Compensation Networks Combating Transformer Parameter Constraints

For a charger with a given three-coil transformer, i.e., given  $M_{PS,PA,SA}$ , the CC output can be varied by tuning the operating frequency or phase shift angle in (3), whereas the CV output in (4) can only be configured either by tuning the magnitude of  $V_A$  or by changing the S(primary)-S(secondary) compensation in the main circuit. In Fig. 1, the variation of  $V_A$  magnitude can be realized only by inserting a circuit before it is connected to the dc source. Therefore, more compensation components are needed to combat the coupler's parameter constraint.

Since the auxiliary side induces a current in the primary coil, the primary side should keep the series compensation to maintain the CC-source driving in CV mode. Thus, the added

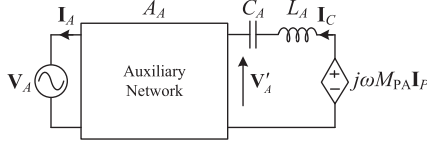


Fig. 3. Equivalent two-port model of the clamp-coil circuit with an auxiliary network  $A_A$ .

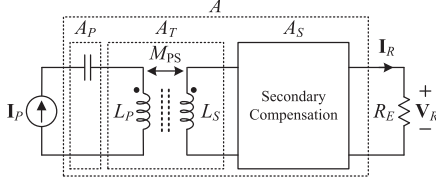


Fig. 4. Equivalent two-port model of the main circuit.

compensation components can only be placed on the auxiliary or secondary sides. These two solutions are discussed as follows.

- 1) An auxiliary network is added after  $V_A$  to produce an ideal voltage source  $V'_A$  with adjustable magnitude, as shown in Fig. 3. The two-port network matrix of the auxiliary network  $A_A$  is defined as  $[\mathbf{V}'_A, \mathbf{I}_C]^T = A_A[\mathbf{V}_A, \mathbf{I}_A]^T$ . For the diode rectifier  $D_{5-8}$ ,  $\mathbf{I}_A$  are in phase with  $\mathbf{V}_A$ . To resemble an ideal voltage source,  $\mathbf{V}'_A$  should be in phase with the current  $\mathbf{I}_C$  flowing the clamp coil. Based on the analysis in [21], the matrix  $A_A$  of the auxiliary network should satisfy

$$A_A = \begin{bmatrix} \frac{1}{E_A} & 0 \\ 0 & E_A^* \end{bmatrix} \quad (5)$$

where  $E_A = \frac{V_A}{V'_A}$  is the voltage gain of the auxiliary network and  $E_A$  is a purely real number, i.e., its complex conjugate  $E_A^* = E_A$ . As  $C_A$  resonant with  $L_A$ ,  $\mathbf{V}'_A = j\omega M_{PA} \mathbf{I}_P$ . Thus, the magnitude regulation of  $\mathbf{V}'_A$  makes the variable  $\mathbf{I}_P$  and the corresponding  $\mathbf{V}_R$  to cope with the battery charging profile.

- 2) If the clamp coil and the series compensation are retained in the auxiliary circuit,  $\mathbf{V}_A$  and its generating  $\mathbf{I}_P$  in CV mode cannot be changed. Then, the S-S compensation in the main circuit cannot meet the requirement of battery profile. Because the series compensation on the primary side should be maintained to guarantee the constant  $\mathbf{I}_P$  driving in CV mode, only the secondary compensation can be modified. As shown in Fig. 4, the main circuit is defined as a two-port network with the matrix  $A$ , where  $[\mathbf{V}_P, \mathbf{I}_P]^T = A[\mathbf{V}_R, \mathbf{I}_R]^T$ . According to [21], the matrix

$A$  should satisfy

$$A = A_P A_T A_S = \begin{bmatrix} 0 & \frac{1}{G} \\ G^* & 0 \end{bmatrix} \quad (6)$$

where  $G = \mathbf{I}_R / \mathbf{V}_P$  is the transconductance of the main circuit, and  $A_P$ ,  $A_T$ , and  $A_S$  are the matrices of primary series compensation, the main coupling of the loosely coupled transformer, and secondary compensation, respectively.  $G$  is a purely imaginary number, i.e.,  $G^* = -G$ . Therefore, the matrix  $A_S$  of the new secondary compensation network should follow (7) shown at the bottom of this page.

Based on the abovementioned analysis, the networks at the auxiliary and secondary sides should be modified as (5) and (7) required. For solution 1), it is well known that a T-type network can realize the reciprocity between an ideal voltage source and an ideal current source [22]. Thus, two cascaded T-type networks are necessary to transmit  $\mathbf{V}_A$  to a magnitude variable  $\mathbf{V}'_A$ , while the matrix of the two cascaded T-networks also satisfies (5). To reduce the number of compensation components, two cascaded T-networks can be further simplified, while there are still many compensation components in the auxiliary circuit [23].

For solution 2), the secondary compensation should satisfy (7). As the auxiliary side is compensated by  $C_A$ , the voltage gain  $E$  for CV charging can be obtained and simplified as (8) with the  $a_{22}$  in (7)

$$E = \frac{\mathbf{V}_R}{\mathbf{V}_A} = \frac{\mathbf{V}_R}{j\omega M_{PA} \mathbf{I}_P} = \frac{1}{j\omega M_{PA} G^*} = \frac{a_{22} M_{PS}}{M_{PA}}. \quad (8)$$

It is clear from (8) that, to make the output voltage adjustable,  $a_{22}$  cannot equal 1, and it should be tunable by changing the compensation parameters of  $A_S$ . The typical first- and second-order secondary compensation networks, including S(series)-type, P(parallel)-type,  $\Gamma$ -type, and reverse  $\Gamma$ -type, are listed in Table I. Among these networks and their matrices, only  $\Gamma$ -type network has the tunable  $a_{22}$  and can be used here. Therefore, three simple topologies with  $\Gamma$ -type secondary network and S-type primary network shown in Fig. 5 can adapt to the configurable output voltage.

This method can be extended to higher-order networks to have more design freedom. A large family of such networks can be deduced in this way and is omitted here.

### C. Design of Proposed $\Gamma$ -Type Secondary Network

The S-LC topology in Fig. 5(a) is taken as an example to analyze the compensation parameters that satisfy the required CC and CV output. The matrix  $A_{LC}$  of the secondary LC

$$\begin{aligned} A_S &= \begin{bmatrix} a_{11} & a_{12} \\ a_{21} & a_{22} \end{bmatrix} = A_T^{-1} A_P^{-1} A = \begin{bmatrix} \frac{L_S}{M_{PS}} & j\omega M_{PS} - j\omega \frac{L_P L_S}{M_{PS}} \\ -\frac{1}{j\omega M_{PS}} & \frac{L_P}{M_{PS}} \end{bmatrix} \cdot \begin{bmatrix} 1 & \frac{-1}{j\omega C_P} \\ 0 & 1 \end{bmatrix} \cdot \begin{bmatrix} 0 & \frac{1}{G} \\ G^* & 0 \end{bmatrix} \\ &= \begin{bmatrix} \frac{G^* L_S}{M_{PS}} \left( \frac{j}{\omega C_P} - j\omega L_P \right) + G^* j\omega M_{PS} & \frac{L_S}{G M_{PS}} \\ \frac{-G^*}{\omega^2 C_P M_{PS}} + \frac{G^* L_P}{M_{PS}} & \frac{-1}{j\omega M_{PS} G} \end{bmatrix}. \end{aligned} \quad (7)$$

TABLE I  
TYPICAL COMPENSATION NETWORKS AND MATRICES

Type	Topology	$A_S$
S-type		$\begin{bmatrix} 1 & Z_S \\ 0 & 1 \end{bmatrix}$
		$\begin{bmatrix} 1 & 0 \\ \frac{1}{Z_P} & 1 \end{bmatrix}$
$\Gamma$ -type		$\begin{bmatrix} 1 & Z_B \\ \frac{1}{Z_A} & 1 + \frac{Z_B}{Z_A} \end{bmatrix}$
		$\begin{bmatrix} 1 + \frac{Z_1}{Z_2} & Z_1 \\ \frac{1}{Z_2} & 1 \end{bmatrix}$

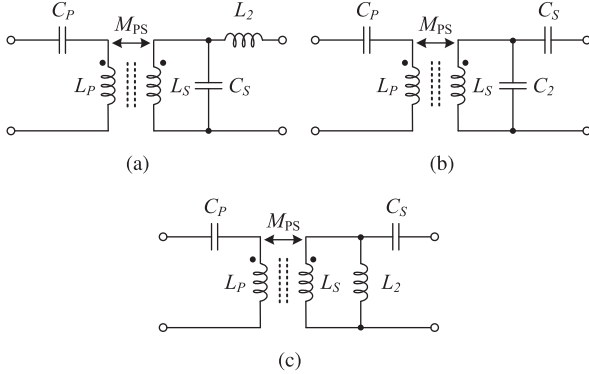


Fig. 5. Three main circuits suitable for three-coil IPT battery charger with S-primary and  $\Gamma$ -secondary compensation. (a) S-LC. (b) S-PS. (c) S-CL.

topology can be expressed as

$$A_{LC} = \begin{bmatrix} 1 & j\omega L_2 \\ j\omega C_S & 1 - \omega^2 L_2 C_S \end{bmatrix}. \quad (9)$$

Substituting (9) into (6) yields the compensation capacitors  $C_P$  and  $C_S$ , which can be calculated as

$$\begin{cases} C_P = \frac{L_S^2}{\omega^2 [L_P L_S^2 - M_{PS}^2 (L_S + L_2)]} \\ C_S = \frac{L_S + L_2}{\omega^2 L_S L_2}. \end{cases} \quad (10)$$

According to (10), the transconductance  $G_{S\_LC}$  for the S-LC topology can be deduced as

$$G_{S\_LC} = \frac{I_R}{V_P} = \frac{jL_S}{\omega M_{PS} L_2}. \quad (11)$$

Thus, the voltage gain  $E_{S\_LC-S}$  considering the clamp circuit for CV charging in (8) can be obtained as

$$E_{S\_LC-S} = \frac{V_R}{V_A} = \frac{1}{j\omega M_{PA} G_{S\_LC}^*} = \frac{M_{PS} L_2}{M_{PA} L_S}. \quad (12)$$

TABLE II  
COMPENSATION PARAMETERS FOR GIVEN VOLTAGE GAIN  $E$

Topology	$C_P$	$C_S$	$L_2$ or $C_2$
S-LC	$\frac{L_S^2}{\omega^2 [L_P L_S^2 - M_{PS}^2 (L_S + L_2)]}$	$\frac{L_S + L_2}{\omega^2 L_S L_2}$	$\frac{E M_{PA} L_S}{M_{PS}}$
S-PS	$\frac{L_S^2 C_2}{\omega^2 L_S C_2 (L_P L_S - M_{PS}^2) + M_{PS}^2}$	$\frac{1}{\omega^2 L_S} - C_2$	$\frac{M_{PS}}{\omega^2 E M_{PA} L_S}$
S-CL	$\frac{L_S^2}{\omega^2 (L_P L_S - M_{PS}^2 + L_P L_2)}$	$\frac{L_S + L_2}{\omega^2 L_S L_2}$	$\frac{E M_{PA} L_S}{M_{PS} - E M_{PA}}$

Based on (11) and (12), the output battery charging CC and CV threshold can be derived as

$$\begin{cases} I_{CC} = \frac{8 L_S V_{dc} \sin \frac{\alpha}{2}}{\pi^2 \omega M_{PS} L_2} \\ V_{CV} = \frac{M_{PS} L_2 V_{dc}}{M_{PA} L_S}. \end{cases} \quad (13)$$

From (13), the output voltage of the charger in CV mode can be configured by tuning the inductor  $L_2$  if the three-coil coupler is given, and the output current in CC mode can be adjusted by changing the operating frequency or phase shift angle like that in [20] to adjust the charging time. Thus, the clamp coil can be designed small and placed inside the primary coil almost without increasing size.

Similarly, the compensation parameters of the other two topologies can be solved by using the abovementioned method and listed in Table II. It is obvious that the voltage gains of both S-PS and S-CL can also be adjusted by changing the parameter of compensation network. To have more design freedom, other higher-order networks, such as T-type and  $\Pi$ -type, can be implemented combating the transformer parameter constraints as well, but more compensation components will be introduced.

So far, the proposed IPT chargers are most suitable for applications that rarely have parameter variation. For example, the parking position of an electric bicycle IPT charger is tightly secured with the help of mechanical structures in [24]. Furthermore, this technology is also suitable for IPT chargers incorporating magnetic couplers with misalignment tolerance, such as double-D pad [25] and bipolar pad [26].

### III. CHARACTERISTICS OF THE S-LC-S-BASED THREE-COIL IPT CHARGER

#### A. Output Characteristic of the S-LC-S-Based Three-Coil IPT Charger

By the abovementioned analysis, the proposed three-coil S(primary)-LC(secondary)-S(auxiliary)-based battery charging system is shown in Fig. 6. With the parameters designed in (10) and (13), the configurable CC and CV can be achieved by assuming the negligible  $M_{SA}$ . Although the clamp coil can be designed small, the existing  $M_{SA}$  and its effect on output performances should be considered. The equivalent circuit of the whole topology is shown in Fig. 7.

Define that  $V_S$  is the vector voltage induced by mutual inductances in the secondary coil and  $I_S$  is the vector current flowing the secondary coil. By Thevenin's theorem, the vectors'



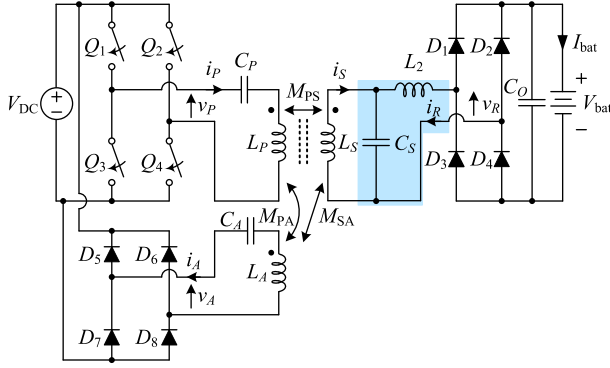


Fig. 6. Proposed S-LC-S-based three-coil IPT battery charger.

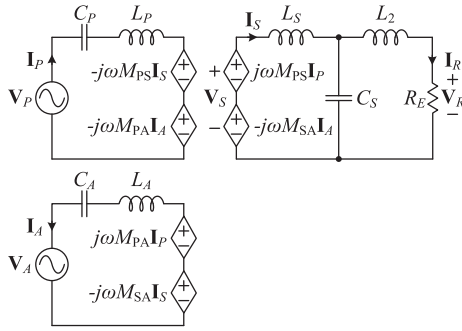


Fig. 7. Equivalent circuit of the proposed S-LC-S-based three-coil IPT battery charger.

relationship in the secondary T network can be obtained as

$$\begin{cases} \mathbf{V}_S = -\frac{L_s}{L_2} \mathbf{V}_R = j\omega M_{PS} \mathbf{I}_P - j\omega M_{SA} \mathbf{I}_A \\ \mathbf{I}_S = j\omega C_s \mathbf{V}_R - \frac{L_2}{L_s} \mathbf{I}_R. \end{cases} \quad (14)$$

Besides, it gives from Fig. 7 as

$$\begin{cases} \mathbf{V}_P = \left(j\omega L_p - \frac{j}{\omega C_p}\right) \mathbf{I}_P - j\omega M_{PS} \mathbf{I}_S - j\omega M_{PA} \mathbf{I}_A \\ \mathbf{V}_R = -\frac{L_2}{L_s} (j\omega M_{PS} \mathbf{I}_P - j\omega M_{SA} \mathbf{I}_A) = \mathbf{I}_R R_E \\ \mathbf{V}_A = j\omega M_{PA} \mathbf{I}_P - j\omega M_{SA} \mathbf{I}_S. \end{cases} \quad (15)$$

In the initial state of charging, the equivalent resistance  $R_L$  is small due to the discharged battery storage, and CC charging starts. Then, the primary current  $\mathbf{I}_P$  and the induced voltage  $\mathbf{V}_A$  rise with the increasing  $R_L$ . Before the amplitude of  $\mathbf{V}_A$  reaches  $V_{dc}$ , i.e.,  $|\mathbf{V}_A| < V_{dc}$ , the diodes  $D_{5-8}$  are OFF and  $i_A = 0$ . Substituting  $\mathbf{I}_A = 0$  into (14) and (15), the output transconductance is same as  $G_{S,LC}$  in (11). The output CC current is as given in (13). Therefore,  $M_{SA}$  cannot affect the CC charging.

Once the peak of  $\mathbf{V}_A$  reaches  $V_{dc}$ , the diodes  $D_{5-8}$  are turned ON partially in one switching period. The CC charging ends and the boundary resistance  $R_{L,\alpha}$  as the ending of CC charging can be derived as (16) by substituting  $|\mathbf{V}_A| = V_{dc}$  into (15)

$$R_{L,\alpha} = \frac{\pi^2 \omega M_{PS}^2 L_2^2}{8 M_{PA} L_s^2 (1 - \Delta)} \sqrt{\frac{\pi^2}{16 \sin^2 \frac{\alpha}{2}} - \frac{M_{SA}^2}{M_{PS}^2}} \quad (16)$$

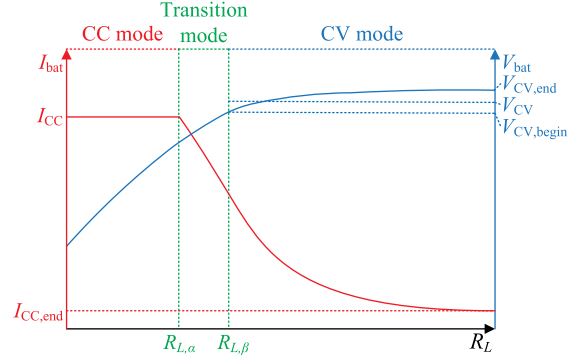


Fig. 8. Diagram of practical charging profile.

where  $\Delta = \frac{M_{PS} M_{SA} (L_s + L_2)}{M_{PA} L_s^2}$ .

With the further increase of  $\mathbf{I}_P$ , the clamp diodes  $D_{5-8}$  are fully conducted and  $\mathbf{V}_A$  is clamped to be a square wave whose fundamental component is constant as  $|\mathbf{V}_A| = \frac{4V_{dc}}{\pi}$ . The other boundary resistance  $R_{L,\beta}$  as the beginning of CV charging is similarly derived from (15) as

$$R_{L,\beta} = \frac{\pi^2 \omega M_{PS}^2 L_2^2}{8 M_{PA} L_s^2 (1 - \Delta)} \sqrt{\frac{1}{\sin^2 \frac{\alpha}{2}} - \frac{M_{SA}^2}{M_{PS}^2}}. \quad (17)$$

Fig. 8 shows the practical charging process of the system with  $R_L$ . If  $R_L > R_{L,\beta}$ , CV charging begins and the ideal  $V_{CV}$  is derived in (13) with the negligible  $M_{SA}$ . In the practical design, the influence of  $M_{SA}$  on the output voltage should be taken into consideration in the following conditions.

- 1) If  $R_L$  is slightly larger than the  $R_{L,\beta}$ , the auxiliary circuit begins to work. Since  $i_A$  is very small at the beginning of CV charging, the insignificant  $i_A$  can be approximated as 0. Substituting (17) into (14) and (15), the output voltage  $V_{CV,begin}$  at  $R_{L,\beta}$  can be derived as

$$V_{CV,begin} = \frac{M_{PS} L_2 V_{dc}}{M_{PA} L_s (1 - \Delta)} \sqrt{1 - \frac{M_{SA}^2}{M_{PS}^2} \sin^2 \frac{\alpha}{2}}. \quad (18)$$

- 2) If  $R_L$  increases far away from  $R_{L,\beta}$ ,  $i_{bat}$  becomes very small and the secondary current  $i_R$  is, thus, insignificant. Here,  $i_R$  can be approximately 0. As  $\mathbf{V}_A$  leads  $\mathbf{I}_P$  a phase of  $90^\circ$ , and  $\mathbf{I}_P$  should be always in phase with  $\mathbf{V}_P$  due to the characteristic of input ZPA. Thus,  $\mathbf{V}_A$  leads  $\mathbf{V}_P$  a phase of  $90^\circ$ . With (14) and (15), the output voltage  $V_{CV,end}$  can be approximately

$$V_{CV,end} = \frac{M_{PS} L_2 V_{dc}}{M_{PA} L_s} \sqrt{1 + \left(\Delta + \frac{M_{SA}}{M_{PS}} \sin \frac{\alpha}{2}\right)^2}. \quad (19)$$

Hence,  $M_{SA}$  has little influence on the output voltage if  $M_{SA} \ll M_{PS}$ . Specifically, the  $M_{SA}$  is required to keep the  $V_{CV,end}$  not exceeding the battery's absolute charging voltage, and to remain  $V_{CV,begin}$  and  $V_{CV,end}$  close.

Besides, if the battery load is accidentally open circuit during the CC mode,  $R_L$  will become infinite and the induced voltage of the clamp coil can be large enough to turn on  $D_{5-8}$ . Then, the

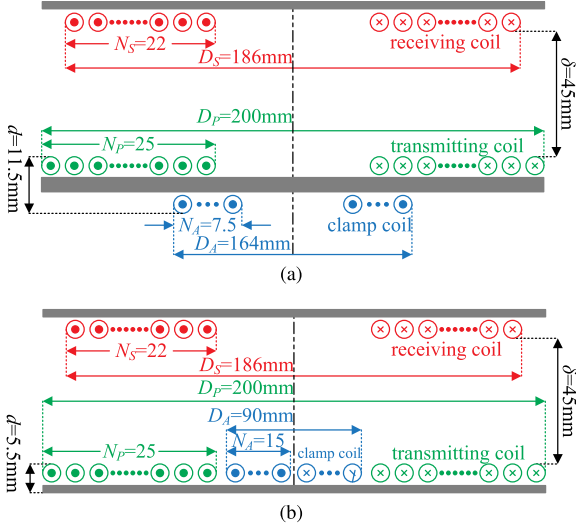


Fig. 9. Winding structure of the couplers. (a) S-S-S-based charger. (b) S-LC-S-based charger.

output voltage will be clamped to  $V_{CV,end}$  and the charging goes to CV mode. Hence, the proposed S-LC-S-based IPT battery charger has an automatic open-circuit protection function.

### B. Performance Comparison With the S-S-S-Based Three-Coil IPT Charger

1) *Magnetic Coupler Design Comparison:* To better compare with the S-S-S-based IPT charger proposed in [20], this article follows the coupler structure with coaxial three circular coils in Fig. 9 where  $D_P$ ,  $D_S$ ,  $D_A$  and  $N_P$ ,  $N_S$ ,  $N_A$  represent the outer diameter and the number of turns for the primary, secondary, and clamp coils, respectively. For both couplers, the primary coil is designed with  $D_P = 200$  mm,  $N_P = 25$  and the secondary coil is designed with  $D_S = 186$  mm,  $N_S = 22$ , with an air gap of  $\delta = 45$  mm between them.

Because the design of the clamp coil for S-S-S-based charger should take the terminal voltage of battery into account, the finite element analysis (FEA) software COMSOL was used to simulate and iterate the design process. On the basis of the FEA iteration simulation results, the clamp coil is designed with  $D_A = 164$  mm and  $N_A = 7.5$ , and is placed under the plane with 7.5-mm thickness to further reduce the  $M_{SA}$ , as shown in Fig. 9(a) [27].

Due to the additional design freedom provided by the secondary LC compensation, the CV output of the S-LC-S-based charger can be controlled by adjusting the inductance  $L_2$  when the  $M_{PS}$  and  $M_{PA}$  are determined. Therefore, to further integrate the coupler, the clamp coil is placed inside the primary coil with  $D_A = 90$  mm and  $N_A = 15$  on a 3.5-mm thick plane, as shown in Fig. 9(b).

Based on the parameters shown in Fig. 9, these two magnetic couplers are actually wound with Litz wire of  $0.1 \text{ mm} \times 200 \text{ mm}$ , and the electrical parameters of which are listed in Table III. These two magnetic couplers are compared in the followings.

1) *Copper consumption of the clamp coil:* Based on the parameters in Fig. 9, the area of clamp coil for the S-S-S

TABLE III  
COUPLERS' ELECTRICAL PARAMETERS FOR DIFFERENT TOPOLOGIES-BASED CHARGERS

Parameters	S-S-S	S-LC-S
$L_P$ ( $\mu\text{H}$ )	119.68	119.84
$L_S$ ( $\mu\text{H}$ )	86.45	86.45
$L_A$ ( $\mu\text{H}$ )	18.63	14.12
$M_{PS}$ ( $\mu\text{H}$ )	29.84	27.4
$M_{PA}$ ( $\mu\text{H}$ )	29.75	12.398
$M_{SA}$ ( $\mu\text{H}$ )	7.065	3.75

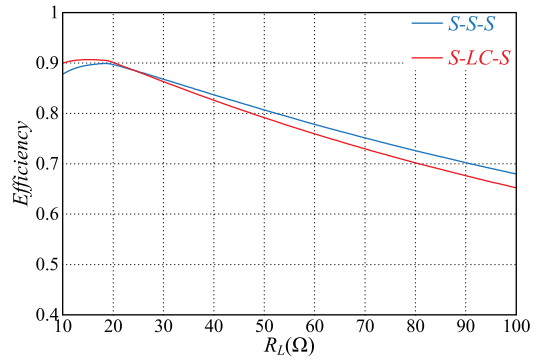


Fig. 10. Efficiency of different topologies-based chargers.

and S-LC-S-based chargers are calculated as 7021 and 5655 mm<sup>2</sup>, respectively. Therefore, the copper consumption of the clamp coil for the S-S-S-based charger is about 1.24 times that for the S-LC-S-based charger.

2) *Volume of the transmitter:* It is obvious that the thickness of transmitter  $d$  for the S-S-S-based charger is about twice that for the S-LC-S-based charger in Fig. 9. In addition, the transmitter for S-S-S-based charger is heavier due to the more copper consumption and the thicker plane.

3) *Mutual inductance  $M_{SA}$ :* As can be seen from the Table III that the  $M_{SA}$  of the coupler for S-LC-S-based charger is only half that for S-S-S-based charger due to the smaller clamp coil. Therefore, in the S-LC-S-based charger, the practical effect of  $M_{SA}$  on the output voltage is smaller.

2) *Efficiency Comparison:* By analyzing the currents of these chargers in different modes, the efficiency of the S-S-S and S-LC-S-based chargers with the same specifications are shown in Fig. 10. It is obvious that the S-LC-S-based charger has higher efficiency than the S-S-S-based charger in CC and transition modes, whereas in CV mode, the reverse is true.

3) *Charging Profile Comparison:* Based on (16), (17) and (10), (13) in [20], curves of the boundary resistances with  $M_{SA}$  for different chargers with the same output voltage are shown in Fig. 11. As the increase of  $M_{SA}$ , the boundary resistances of the S-LC-S-based charger gradually increase, whereas those of the S-S-S-based charger gradually decrease. This suggests

TABLE IV  
COMPARISON OF THE IPT CHARGER WITH SELF-SUSTAINED BATTERY CHARGING PROFILE

Paper reference	This work	[20]	[23]	[19]
Auxiliary circuit location	Transmitter	Transmitter	Transmitter	Receiver
Number of transmitter's compensation components	2	2	5	1
Number of receiver's compensation components	2	1	1	4
CV output combating transformer parameter constraints	YES	NO	YES	YES
CC output combating transformer parameter constraints	YES	NO	NO	NO

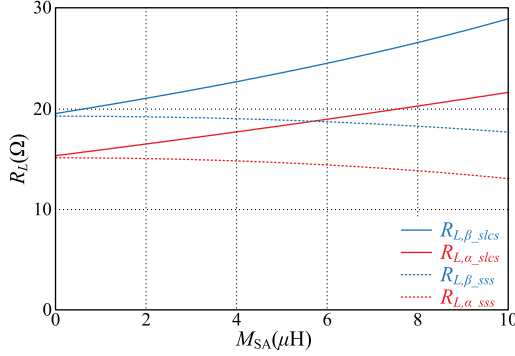


Fig. 11. Boundary resistances versus  $M_{SA}$  for different topologies-based chargers.

that the S-S-S-based charger enters the transition and CV modes earlier than the S-LC-S-based charger, resulting in a longer charging duration.

4) *Comparison With Other Works*: To compare the work in this article with other IPT chargers with self-sustained charging profiles, Table IV summarizes these articles from the perspective of auxiliary circuit location, number of compensation components, etc. It is clear that both the CC and CV outputs of the S-LC-S-based charger are free from the constraints of the magnetic coupler. In addition, compared with the charger proposed in [19] and [23] that also allow for adjustable CV output, the chargers proposed in this article only add an additional compensation component on the secondary side that has a minimal impact on the weight of the receiver.

#### IV. EXPERIMENTAL VERIFICATIONS

To verify the abovementioned analysis, an IPT prototype is built in the laboratory to charge a 15S 48 V/20 Ah lithium iron phosphate battery, as shown in Fig. 12. The MOSFETs and diodes in the prototype are IRF640 and MBR20200 separately. All waveforms are recorded by Tektronix DPO 2024 Oscilloscope. Power and efficiency are measured by YOKOGAWA WT1085E. The phase shift angle  $\alpha$  of the DSP TMS320F28335 controlled inverter is set as  $0.95\pi$ . The input voltage  $V_{dc}$  is 48 V and an electronic load Chroma 63112 A emulates the battery for different charging modes. According to [28], the overdischarge protection voltage, CV charging voltage, absolute charging voltage, and cutoff current of a single cell are 2, 3.65, 3.8, and 0.5 A, respectively. Thus, the charging process of the 15S battery with the proposed charger starts at  $2 \times 15 = 30$  V terminal voltage with 2.5 A constant charging current and ends at 0.5 A charging current with  $3.65 \times 15 = 54.75$  V constant charging voltage.

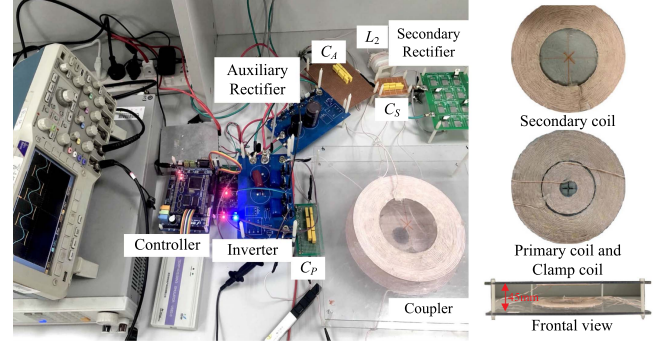


Fig. 12. Photograph of the experimental prototype.

During the CC and transition modes, the voltage of the battery increases with the SOC of the battery. While in CV mode, the charging current decreases as the battery's SOC increases. As a result, the equivalent resistance of the battery increases slowly from 12 to 109.5  $\Omega$  with the SOC in each mode. In order to facilitate the simulation of batteries with electronic loads, the equivalent resistance range of the battery is simplified from [12  $\Omega$ , 109.5  $\Omega$ ] to [10  $\Omega$ , 100  $\Omega$ ] for the prototype.

As the operating frequency is set as 200 kHz,  $C_P$ ,  $C_S$ ,  $C_A$ , and  $L_2$  are 6.11 nF, 23.82 nF, 44.98 nF, and 39.4  $\mu$ H from (10) and (13). By (16) and (17), the boundary resistances  $R_{L,\alpha}$  and  $R_{L,\beta}$  are calculated as 17.3 and 22.1  $\Omega$ , respectively. In total, three charging conditions with  $R_L$  of 10, 20, and 100  $\Omega$  are given here to demonstrate the charging performance in CC, transition, and CV modes. Fig. 13 gives the experimental waveforms of primary voltage  $v_P$ , primary current  $i_P$ , secondary voltage  $v_R$ , and secondary current  $i_R$  for three modes. It is obvious that  $i_P$  is always slightly lagging to  $v_P$  to ensure the zero-voltage switching turn-ON of  $Q_{1-4}$  and nearly zero reactive power of the circuit in the whole charging process. Fig. 14 shows the experimental waveforms of auxiliary voltage  $v_A$ , auxiliary current  $i_A$ , battery voltage  $V_{bat}$ , and battery current  $I_{bat}$  at different modes. Due to  $R_L < R_{L,\alpha}$  in Fig. 14(a), the charger is operated in CC mode and there is an induced potential  $v_A$  on the clamp coil, which is not large enough to turn ON the auxiliary rectifier bridge  $D_{5-8}$ , i.e.,  $i_A = 0$ . The output current  $I_{bat}$  is measured as about 2.5 A, consistent to (13) and satisfying the required CC output. With the  $R_L$  increasing to Fig. 14(b), the induced  $v_A$  will partially exceed  $V_{dc}$  and then be clamped to  $V_{dc}$ . The auxiliary rectifier bridge is not fully activated and  $i_A$  is discontinuous. This is the CC-to-CV transition mode with the output voltage  $V_{bat}$  of about 46 V. Until  $R_L > R_{L,\beta}$  in Fig. 14(c),  $v_A$  is totally clamped to



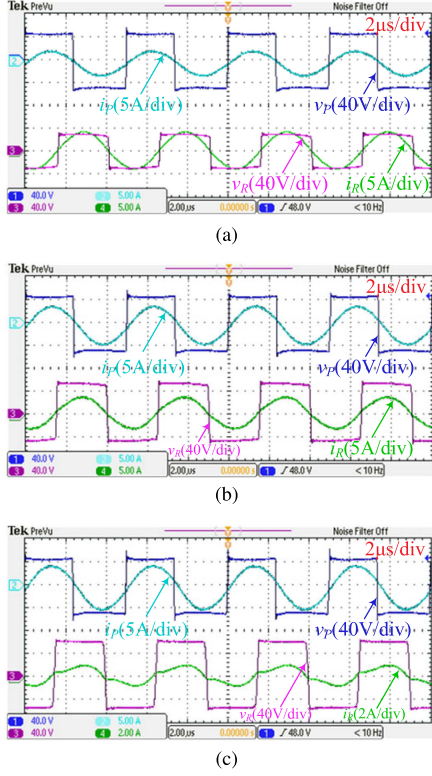


Fig. 13. Experimental waveforms of  $v_P$ ,  $i_P$ ,  $v_R$ , and  $i_R$  for (a) CC mode ( $R_L = 10 \Omega$ ), (b) transition mode ( $R_L = 20 \Omega$ ), and (c) CV mode ( $R_L = 100 \Omega$ ).

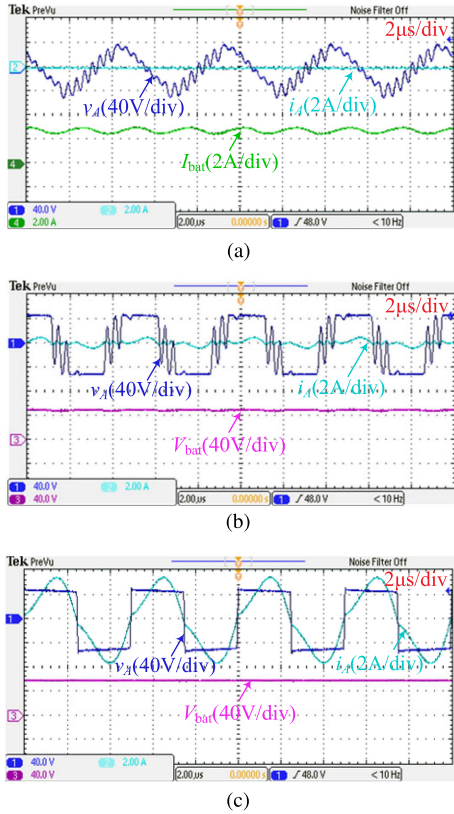


Fig. 14. Experimental waveforms of  $u_A$ ,  $i_A$ , and  $I_{bat}$  ( $V_{bat}$ ) for (a) CC mode ( $R_L = 10 \Omega$ ), (b) transition mode ( $R_L = 20 \Omega$ ), and (c) CV mode ( $R_L = 100 \Omega$ ).

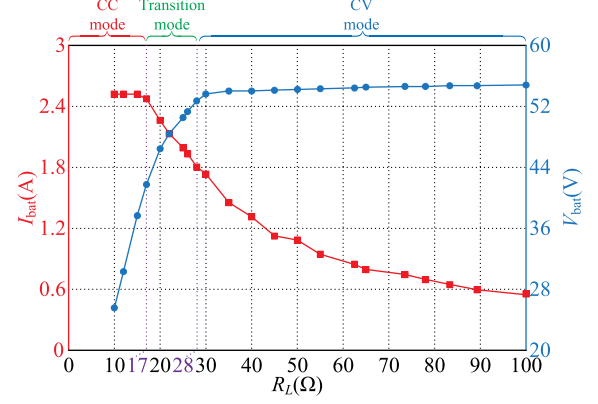


Fig. 15. Measured  $I_{bat}$  and  $V_{bat}$  versus  $R_L$ .

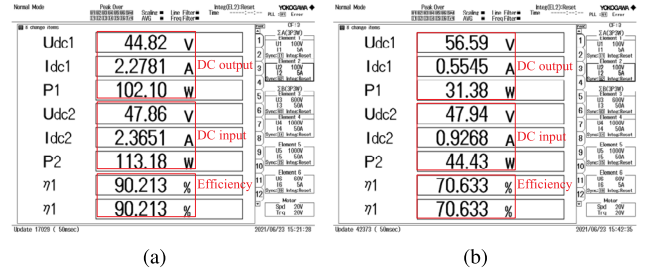


Fig. 16. Screenshots of the power analyzer at (a)  $R_b = 20 \Omega$  and (b)  $R_b = 100 \Omega$ .

$V_{dc}$  and  $i_A$  current is continuous. The IPT charger is operated in CV mode with  $V_{bat}$  close to  $V_{CV,end}$  in (19).

Fig. 15 shows the curves of measured battery voltage  $V_{bat}$  and current  $I_{bat}$  versus the battery equivalent load resistance  $R_L$ . With the coupler in Table III and parameter design in Section III-B, the required CC and CV outputs of the system can be achieved for the configurable battery charging profile with a small clamp coil. The tolerance of  $R_{L,\beta}$  in this figure is caused by the assumption of  $i_A = 0$  at the beginning of CV charging, where the discontinuous  $i_A$  exists in the transition mode, as shown in Fig. 14(b).

A precise power analyzer is used to measure the input power, output power, and efficiency of the system. The screenshots of measured results with  $R_L = 20 \Omega$  and  $R_L = 100 \Omega$  are shown in Fig. 16. Fig. 17 plots the efficiency curve of the IPT battery charger versus  $R_L$ . The maximum efficiency is about 90.35% near  $R_L = 17 \Omega$ , where the auxiliary diodes do not fully conduct and the current  $i_A$  is almost zero, such that the losses caused by the auxiliary circuit are smaller. The significant efficiency penalty in the late CV stage (light load conditions) is owing to the reflow current of the auxiliary circuit  $I_A$  increasing with the decrease of output power. However, since the power transferred by the proposed charger during the CV mode is less than 20% of the entire charging process [29], the efficiency penalty is acceptable.

This article's future scope focuses on the following two aspects. The first is to improve the chargers' efficiency by adopting GaN and SiC devices with lower drain-source on-resistance



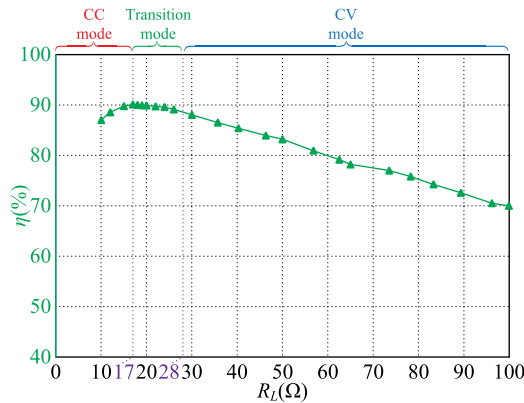


Fig. 17. Measured efficiency  $\eta$  versus  $R_L$ .

or forward voltage, and the second is to enhance the chargers' misalignment tolerance by combining the novel magnetic couplers.

## V. CONCLUSION

To self-sustain the battery with a configurable charging profile, a novel family of three-coil IPT battery chargers is proposed in this article featuring the automatic CC-to-CV transition with a small clamp coil in the transmitter. With an additional inductor or capacitor added on the secondary side, the parameter constraint of the coupler is combated and the clamp coil can be designed very small to be placed inside the primary coil, which almost does not increase the volume of the magnetic coupler. Moreover, the proposed charger can also inherit all advantages of the three-coil structure, such as near unity power factor, soft switching, and open-circuit protection. The experiment results agree with the theoretical analysis well.

## REFERENCES

- [1] S. Y. Hui, "Planar wireless charging technology for portable electronic products and Qi," *Proc. IEEE*, vol. 101, no. 6, pp. 1290–1301, Jun. 2013.
- [2] P. S. Riehl et al., "Wireless power systems for mobile devices supporting inductive and resonant operating modes," *IEEE Trans. Microw. Theory Techn.*, vol. 63, no. 3, pp. 780–790, Mar. 2015.
- [3] O. Knecht and J. W. Kolar, "Performance evaluation of series-compensated IPT systems for transcutaneous energy transfer," *IEEE Trans. Power Electron.*, vol. 34, no. 1, pp. 438–451, Jan. 2019.
- [4] M. R. Basar, M. Y. Ahmad, J. Cho, and F. Ibrahim, "An improved wearable resonant wireless power transfer system for biomedical capsule endoscope," *IEEE Trans. Ind. Electron.*, vol. 65, no. 10, pp. 7772–7781, Oct. 2018.
- [5] G. Buja, M. Bertoluzzo, and K. N. Mude, "Design and experimentation of WPT charger for electric city car," *IEEE Trans. Ind. Electron.*, vol. 62, no. 12, pp. 7436–7447, Dec. 2015.
- [6] L. Zhao, D. J. Thrimawithana, U. K. Madawala, A. P. Hu, and C. C. Mi, "A misalignment-tolerant series-hybrid wireless EV charging system with integrated magnetics," *IEEE Trans. Power Electron.*, vol. 34, no. 2, pp. 1276–1285, Feb. 2019.
- [7] T. Orecan, P. Zhang, and C. Shih, "Analysis, design, and maximum power-efficiency tracking for undersea wireless power transfer," *IEEE J. Emerg. Sel. Topics Power Electron.*, vol. 6, no. 2, pp. 843–854, Jun. 2018.
- [8] C. Zhang, D. Lin, N. Tang, and S. Y. R. Hui, "A novel electric insulation string structure with high-voltage insulation and wireless power transfer capabilities," *IEEE Trans. Power Electron.*, vol. 33, no. 1, pp. 87–96, Jan. 2018.
- [9] S. Zhao et al., "A 4 kV/120 A SiC solid-state DC circuit breaker powered by a load-independent IPT system," *IEEE Trans. Ind. Appl.*, vol. 58, no. 1, pp. 1115–1125, Jan./Feb. 2022.
- [10] W. Zhang and C. C. Mi, "Compensation topologies of high-power wireless power transfer systems," *IEEE Trans. Veh. Technol.*, vol. 65, no. 6, pp. 4768–4778, Jun. 2016.
- [11] C. Chen et al., "Modeling and decoupled control of inductive power transfer to implement constant current/voltage charging and ZVS operating for electric vehicles," *IEEE Access*, vol. 6, pp. 59917–59928, 2018.
- [12] Z. Li et al., "A 3-kW wireless power transfer system for sightseeing car supercapacitor charge," *IEEE Trans. Power Electron.*, vol. 32, no. 5, pp. 3301–3316, May 2017.
- [13] R. Mai, Y. Chen, Y. Li, Y. Zhang, G. Cao, and Z. He, "Inductive power transfer for massive electric bicycles charging based on hybrid topology switching with a single inverter," *IEEE Trans. Power Electron.*, vol. 32, no. 8, pp. 5897–5906, Aug. 2017.
- [14] Y. Li, J. Hu, F. Chen, S. Liu, Z. Yan, and Z. He, "A new-variable-coil-structure-based IPT system with load-independent constant output current or voltage for charging electric bicycles," *IEEE Trans. Power Electron.*, vol. 33, no. 10, pp. 8226–8230, Oct. 2018.
- [15] V. B. Vu, D. H. Tran, and W. Choi, "Implementation of the constant current and constant voltage charge of inductive power transfer systems with the double-sided LCC compensation topology for electric vehicle battery charge applications," *IEEE Trans. Power Electron.*, vol. 33, no. 9, pp. 7398–7410, Sep. 2018.
- [16] J. Lu, G. Zhu, D. Lin, Y. Zhang, J. Jiang, and C. C. Mi, "Unified load-independent ZPA analysis and design in CC and CV modes of higher order resonant circuits for WPT systems," *IEEE Trans. Transport. Electrification*, vol. 5, no. 4, pp. 977–987, Dec. 2019.
- [17] Z. Zhang, F. Zhu, D. Xu, P. T. Krein, and H. Ma, "An integrated inductive power transfer system design with a variable inductor for misalignment tolerance and battery charging applications," *IEEE Trans. Power Electron.*, vol. 35, no. 11, pp. 11544–11556, Nov. 2020.
- [18] J. Tian and A. P. Hu, "A DC-voltage-controlled variable capacitor for stabilizing the ZVS frequency of a resonant converter for wireless power transfer," *IEEE Trans. Power Electron.*, vol. 32, no. 3, pp. 2312–2318, Mar. 2017.
- [19] G. Li and H. Ma, "A hybrid IPT system with high-misalignment tolerance and inherent CC–CV output characteristics for EVs charging applications," *IEEE J. Emerg. Sel. Topics Power Electron.*, vol. 10, no. 3, pp. 3152–3160, Jun. 2022.
- [20] Z. Huang, G. Wang, J. Yu, and X. Qu, "A novel clamp coil assisted IPT battery charger with inherent CC-to-CV transition capability," *IEEE Trans. Power Electron.*, vol. 36, no. 8, pp. 8607–8611, Aug. 2021.
- [21] X. Qu, Y. Jing, H. Han, S. C. Wong, and C. K. Tse, "Higher order compensation for inductive-power-transfer converters with constant-voltage or constant-current output combating transformer parameter constraints," *IEEE Trans. Power Electron.*, vol. 32, no. 1, pp. 394–405, Jan. 2017.
- [22] M. Borage, K. V. Nagesh, M. S. Bhatia, and S. Tiwari, "Resonant immittance converter topologies," *IEEE Trans. Ind. Electron.*, vol. 58, no. 3, pp. 971–978, Mar. 2011.
- [23] R. Yao, X. Qu, J. Yu, G. Wang, and W. Chen, "Three-coil wireless battery charger with self-adaptation to battery charging curve (in Chinese)," *Autom. Electric Power Syst.*, vol. 46, no. 7, pp. 170–177, Apr. 2022.
- [24] R. Mai, Y. Chen, Y. Zhang, N. Yang, G. Cao, and Z. He, "Optimization of the passive components for an S-LCC topology-based WPT system for charging massive electric bicycles," *IEEE Trans. Ind. Electron.*, vol. 65, no. 7, pp. 5497–5508, Jul. 2018.
- [25] M. Budhia, J. T. Boys, G. A. Covic, and C.-Y. Huang, "Development of a single-sided flux magnetic coupler for electric vehicle IPT charging systems," *IEEE Trans. Ind. Electron.*, vol. 60, no. 1, pp. 318–328, Jan. 2013.
- [26] A. Zaheer, H. Hao, G. A. Covic, and D. Kacprzak, "Investigation of multiple decoupled coil primary pad topologies in lumped IPT systems for interoperable electric vehicle charging," *IEEE Trans. Power Electron.*, vol. 30, no. 4, pp. 1937–1955, Apr. 2015.
- [27] G. Wang, "A three-coil wireless battery charger with inherent CC-to-CV transition capability," M.S. thesis, Sch. Elect. Eng., Southeast Univ., Nanjing, China, Jun. 2021.
- [28] China Aviation Lithium Battery, "Product specification: Prismatic lithium-ion battery," *Better Technol. Group Ltd., Xiamen, China, SE200F-I datasheet*, Aug. 2016.
- [29] A. Al-Haj Hussein and I. Batarseh, "A review of charging algorithms for nickel and lithium battery chargers," *IEEE Trans. Veh. Technol.*, vol. 60, no. 3, pp. 830–838, Mar. 2011.



**Chunwei Ma** (Student Member, IEEE) received the B.Eng. degree in electrical engineering from the Nanjing Institute of Technology, Nanjing, China, in 2017, and the M.Eng. degree in electrical engineering from the Nanjing University of Science and Technology, Nanjing, China, in 2020. He is currently working toward the Ph.D. degree in electrical engineering with Southeast University, Nanjing, China.

From 2020 to 2021, he was a Hardware Engineer with Da-Jiang Innovations, Shenzhen, China. His current research interests include wireless power transfer, power factor correction converters, and motor drives.



**Cheng Li** received the B.Eng. degree in electrical engineering from Southwest Jiaotong University, Chengdu, China, in 2022. He is currently working toward the M.Eng. degree in electrical engineering with Southeast University, Nanjing, China.

His research focuses on wireless power transfer.



**Ruoyu Yao** received the B.Eng. degree in electrical engineering from Northeast Electric Power University, Jilin, China, in 2019, and the M.Eng. degree in electrical engineering from Southeast University, Nanjing, China, in 2022.

Since 2022, she has been with the State Grid Shanghai Pudong Electric Power Supply Company, Shanghai, China. Her current research interests include wireless power transfer and stability analysis of dc microgrids.



**Xiaohui Qu** (Senior Member, IEEE) received the B.Eng. and M.Eng. degrees in electrical engineering from the Nanjing University of Aeronautics and Astronautics, Nanjing, China, in 2003 and 2006, respectively, and the Ph.D. degree in power electronics from Hong Kong Polytechnic University, Hong Kong, in 2010.

From February to May 2009, she was a Visiting Scholar with the Center for Power Electronics Systems, Virginia Tech, Blacksburg, VA, USA. Since 2010, she has been with the School of Electrical

Engineering, Southeast University, Nanjing, China, where she is currently a Full Professor with research focus on power electronics. From January 2015 to January 2016, she was a Visiting Scholar with the Center of Reliable Power Electronics, Aalborg University, Aalborg, Denmark. Her current research interests include wireless power transfer, flexible ac/dc distribution power system, and power electronics reliability.

Dr. Qu was the recipient of the Outstanding Reviewer Award and Prize Paper Award from IEEE TRANSACTIONS ON POWER ELECTRONICS in 2017 and 2018, respectively.